Mesoscopic-Scale Numerical Simulation Including the Influence of Process Parameters on SLM Single-Layer Multi-pass Formation

LIU CAO

Selective laser melting (SLM) is a metal additive manufacturing technology that directly forms three-dimensional complex components according to digital models *via* layer-by-layer addition. It has been widely used in medical personalization, aerospace, and other fields. To analyze the influence of different process parameters, such as the line energy density and hatch space on the SLM single-layer multi-pass formation process, a random particle distribution of the powder bed was first obtained *via* the open-source discrete element method (DEM) code Yade. The prediction model of the molten pool dynamic behavior during the SLM formation process was then established based on the ''metal-gas'' two-phase flow model. The conservation equation considered thermal factors, such as the Marangoni effect, the porosity in the mushy zone, and the gasification phenomenon. Laser energy was then applied by the body heat source model, which directly tracked the metal-phase surface affected by the laser in real time and applied energy to the metal-phase elements within a certain thickness. By analyzing the simulation results, it was found that to obtain a good formation zone in actual SLM production for 316L stainless steel, from the perspective of controlling line energy density, 200 J/m should be used to obtain a relatively flat solidified track and to establish a good connection with the substrate or the upper formation layer; from the perspective of controlling the hatch space, 45 μm should be used to ensure a good connection between adjacent solidified tracks, a relatively flat formation surface, and high production efficiency. These conclusions were consistent with the experimental results. This article offers a scientific rationale for parameter selection during the SLM formation process of 316L stainless steel.

https://doi.org/10.1007/s11661-020-05831-z

I. INTRODUCTION

SELECTIVE laser melting (SLM) is a metal additive manufacturing technology that uses a laser as an energy source and metal powder as raw material to form three-dimensional complex parts *via* a digital model and layer-by-layer methods. It is widely used in personalized medical devices, conformal cooling molds, aerospace, and other fields.[1] The SLM formation process is a strong non-equilibrium thermal process. The complex molten pool dynamics and phase transitions are quite different from traditional thermal processing.[2] There are currently formation defects such as pores, warpage deformation, residual stress, and poor microstructures in SLM industrial production,[3,4] which greatly restrict the further use of SLM.

Many experimental studies have been done on SLM, mainly involving in suit observations of the formation process,[5,6] defect detection,[7] process parameters analysis (laser power, scanning speed, hatch space, layer thickness, scanning strategy, placement orientation, *etc.*),[8–13] mechanical performance control (tensile strength, elongation, hardness, wear property, corrosion resistance, erosion property, *etc.*),[14–16] structural topology optimization,[17,18] effect of particle additions on mechanical properties,[19,20] lattice structure,[21] and functionally graded material.[22] Martin *et al.*[23] used *in situ* X-ray imaging to observe the formation of pores during the SLM process. The collapse of deep keyhole depressions caused by the deceleration and acceleration of the scanning mirrors during the turn was the main cause of pore defects. Sing *et al.*[24] studied the effects of process parameters such as laser power and scanning speed on the properties of components such as density, hardness, and surface roughness for the SLM formation process of titanium-tantalum alloys. Andreau *et al.*[25] studied the correlation between the melt-pool geometry

LIU CAO is with the Advanced Institute of Engineering Science for Intelligent Manufacturing, Guangzhou University, Guangzhou 510006, Guangdong, People's Republic of China. Contact e-mail: caoliu@gzhu.edu.cn

Manuscript submitted October 19, 2019.
Article published online May 29, 2020

and the resulting texture and found that the decrease in the melt pool depth was assumed to be linked to the local attenuation of the laser beam effective power density transmitted to the powder bed. These experimental results were useful in understanding the SLM formation mechanism.

Numerical simulation is a quantitative and time-saving analysis method. It is an important supplement and extension of experimental research for obtaining characteristic data during the entire formation process, including the three-dimensional morphology of the molten pool and the grain evolution behavior during solidification, and it has been gradually applied to the prediction and optimization of the SLM formation process.[26] Current simulation studies for SLM technology are mainly divided into three scales: macroscopic,[27–29] mesoscopic,[30] and microscopic.[31] Macroscopic-scale research works require the treatment of the powder bed to be a continuous medium to obtain the temperature and stress evolution of SLM components.[32–34] Mesoscopic-scale studies directly describe the complex molten pool dynamics of metal particles after laser heating and accurately reproduce the gas-liquid-solid complex and coupling behavior during the SLM process,[35] and these features are the focus of this article. Microscopic-scale studies focus on the microstructure evolution at high solidification rates and cooling rates during the SLM process.[36]

Mesoscopic-scale research describes the interaction between metal particles and the laser. Thus, the simulations were mainly divided into two parts: particle distribution of the powder bed[37,38] and molten pool dynamics.[39,40] Nan *et al.*[41] predicted the particle distribution of the spreading process based on the discrete element method (DEM) and analyzed the effects of the spreading rate and the gap height on the particle velocity and mass flow rate. The particle velocity in front of the blade could be described by a universal curve given by the Gauss error function. Tang *et al.*[42] studied the effects of surface tension and gasification recoil on pore defects during the SLM formation process based on the open-source computational fluid dynamics (CFD) code OpenFOAM. Later work[43] carried out SLM simulations at the mesoscopic scale from three aspects: particle size distribution, powder bed packing density, and thickness. The results showed that to obtain a good formation zone, the quantity percentage of large-diameter particles in the powder should be minimized to avoid the rough formation surface. Simulations can provide a good foundation for the scientific description of the SLM process, but further studies are needed such as the influence of hatch space on the surface roughness of the formation zone.

To analyze the influence of different process parameters such as line energy density and hatch space on the SLM single-layer multi-pass formation process, the random particle distribution of the powder bed was obtained by DEM. The prediction model of the molten pool dynamic behavior was then established based on the "metal-gas" two-phase flow model. The conservation equation considered the thermal factors, such as the Marangoni effect, the porosity in the mushy zone, and the gasification phenomenon. The laser energy was applied by the body heat source model, which tracked the metal-phase surface directly affected by the laser in real time, and then applied energy to the metal-phase elements of a certain thickness. This article provides a scientific basis for the parameter selection used during SLM of 316L stainless steel.

II. PHYSICAL MODELING AND NUMERICAL SOLUTION

A. *Random Particles Distribution*

The basis of the mesoscopic-scale study on the SLM formation process is to obtain the particle distribution of the powder bed. The work is composed of two types of information: particle size and particle position. The particle size distribution must use experimental methods to measure the particle radius. The data were fit with a special function (such as a normal distribution). The particle position information was obtained by DEM, and the core idea was that each particle had translational and rotational freedom and met Newton's law of motion. The random distribution of the metal particles during the spreading process was obtained *via* equivalent treating of the interactions between the particles or the particle and the blade/roller. The distribution of particles in the powder bed was predicted based on the open-source DEM code Yade[44] wherein the particle size distribution conformed to a normal distribution. The particles were considered spherical, and the particle contact force model adopted the soft ball model[45]; the particle density was set to 7650 kg/m^3, the contact friction angle was set to 0.3, Poisson's ratio was set to 0.34, Young's modulus was set to 195 GPa, and other parameters adopted the default Yade settings.

B. *Molten Pool Dynamics Model*

The metal particles are melted by laser heating to form a molten pool during the SLM formation process. The molten pool undergoes intense convection and shape change under the combined effects of surface tension, the Marangoni effect, and gasification recoil. The molten pool then gradually solidifies to form a solidified track and forms a metallurgical bond with the metal substrate or the upper formation layer. Figure 1 shows a schematic diagram of the SLM formation process. To ensure the stability and efficiency of the numerical solution, the following three assumptions were made: ignoring the influence of metal density change on volume, ignoring the influence of metal liquid gasification on alloy composition, and considering the flow of liquid metal and protective gas satisfying the laminar flow condition of an incompressible Newtonian fluid.

Describing the SLM formation process based on the mesoscopic scale means that the interface between the metal and the protective gas needs to be characterized in real time. In this article, the volume ratio factor α_1 was used to represent the percentage of the metal phase in

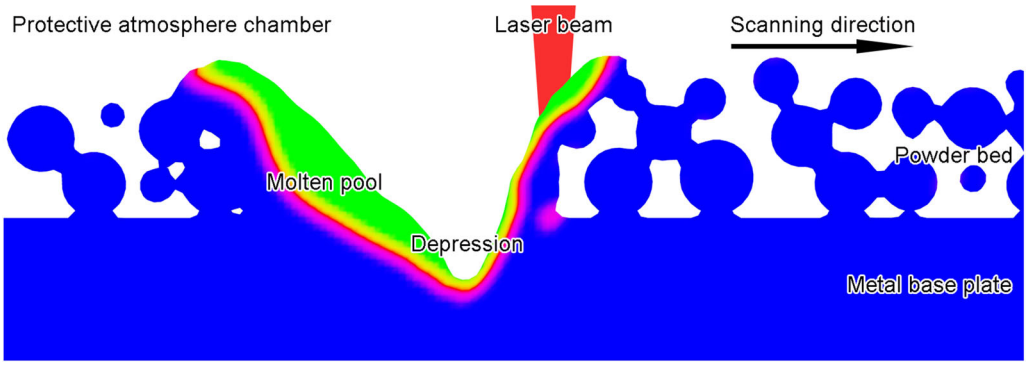

Fig. 1—Schematic diagram of the SLM formation process.

Table I. Main Thermal Factors Influencing the SLM Formation Process

Factor	Expression	Number
Pressure	$\vec{F}_{\text{pressure}} = -\nabla p$	[3]
Viscous Force	$\vec{F}_{\text{viscous}} = \nabla \cdot \left\{ 2\bar{\mu} \left[\left(\frac{1}{2}\nabla\vec{u} + \frac{1}{2}\left(\nabla\vec{u}\right)^T \right) - \frac{1}{3}\left(\nabla \cdot \vec{u}\right)\mathbf{I} \right] \right\}$	[4]
Gravity	$\vec{F}_{\text{gravity}} = \bar{\rho}\vec{g}$	[5]
Drag Force of Mushy Zone	$\vec{F}_{\text{mushy}} = -\bar{\rho}K_C \left[\frac{\left(1-f_{\text{liquid}}\right)^2}{f_{\text{liquid}}^3 + C_K} \right] \vec{u}$	[6]
Surface Tension	$\vec{F}_{\text{tension}} = \sigma\kappa\vec{n}$	[7]
Marangoni Effect	$\vec{F}_{\text{Marangoni}} = \frac{d\sigma}{dT}\left[\nabla T - \vec{n}\left(\vec{n} \cdot \nabla T\right)\right]$	[8]
Gasification Recoil Force	$\vec{F}_{\text{recoil}} = 0.54P_0 \exp\left[\frac{L_v m}{k_B}\left(\frac{1}{T_v} - \frac{1}{T}\right)\right]\vec{n}$	[9]
Convection Heat Dissipation	$q_{\text{con}} = h_{\text{con}}\left(T - T_{\text{con}}\right)$	[10]
Radiation Heat Dissipation	$q_{\text{rad}} = \sigma_s \varepsilon \left(T^4 - T_{\text{rad}}^4\right)$	[11]
Gasification Heat Dissipation	$q_{\text{vap}} = 0.82\frac{L_v m}{\sqrt{2\pi m k_B T}} P_0 \exp\left[\frac{L_v m}{k_B}\left(\frac{1}{T_v} - \frac{1}{T}\right)\right]$	[12]

the element, and the interface between the metal-phase and the gas-phase could be determined by the elements with α_1 values between zero and one. The VOF model[46] was used to control the α_1 distribution and is shown below:

$$\frac{\partial \alpha_1}{\partial t} + \nabla \cdot \left(\alpha_1 \vec{u}\right) = 0 \qquad [1]$$

$$\alpha_1 + \alpha_2 = 1 \qquad [2]$$

Here, α_1, α_2 are the element volume fractions of the metal phase and the gas phase, respectively; t is the time, s; $\vec{u}$ is the velocity, m/s.

From the perspective of CFD, the complexity of the dynamic behavior of the molten pool during the SLM process is reflected in complex thermal factors. Table I lists the main thermal factors influencing the SLM formation process[42,43]:

In Table I:

$$\bar{\rho} = \alpha_1\rho_1 + \alpha_2\rho_2 \qquad [13]$$

$$\vec{n} = \frac{\nabla \alpha_1}{|\nabla \alpha_1|} \qquad [14]$$

$$\kappa = -\nabla \cdot \vec{n} \qquad [15]$$

where p is the pressure, Pa; $\bar{\rho}$, ρ_1, ρ_2 are the mixed, metal-phase, and gas-phase densities, respectively, kg/m^3; $\bar{\mu}$ is the mixed dynamic viscosity, Pa s; $\mathbf{I}$ is the unit matrix; $\vec{g}$ is the gravitational acceleration, m/s^2; K_C is the drag coefficient of mushy zone,[47] and its value was set to 10 herein, 1/s; f_{liquid} is the liquid fraction of metal phase; C_K is a custom small value, such as 1e^{-2}; σ is the surface tension coefficient, N/m; κ is the interface curvature, 1/m; $\vec{n}$ is the unit normal vector on the interface; T is the temperature, K; $\frac{d\sigma}{dT}$ is the rate of change of σ with temperature, N/(m K); P_0 is the atmospheric pressure, Pa; L_v is the gasification latent heat, J/kg; m is the metal molecular mass, kg; k_B is the Boltzmann constant, J/K; T_v is the metal gasification temperature, K; h_{con} is the convective heat transfer coefficient, W/(m^2 K); T_{con} is the external convection temperature, K; σ_s is the Stefan–Boltzmann constant,

W/(m^2 K^4); ε is the emissivity; T_{rad} is the external radiation temperature, K.

The three types of conservation equations for momentum, energy, and mass that control the dynamic behavior of the SLM molten pool are shown below:

$$\frac{\partial \bar{\rho}\vec{u}}{\partial t} + \nabla \cdot \left(\bar{\rho}\vec{u} \otimes \vec{u}\right) = \vec{F}_{pressure} + \vec{F}_{viscous} + \vec{F}_{gravity} + \vec{F}_{mushy} + \left(\vec{F}_{tension} + \vec{F}_{Marangoni} + \vec{F}_{recoil}\right)\left|\nabla \alpha_1\right| \frac{2\bar{\rho}}{\rho_1 + \rho_2} \quad [16]$$

$$\frac{\partial \bar{\rho}\bar{c}_e T}{\partial t} + \nabla \cdot \left(\bar{\rho}\vec{u}\bar{c}_e T\right) - \nabla \cdot \left(\bar{k}\nabla T\right) = -\left(q_{\text{con}} + q_{\text{rad}} + q_{\text{vap}}\right)\left|\nabla \alpha_1\right| \frac{2\bar{\rho}\bar{c}_e}{\rho_1 c_1 + \rho_2 c_2} + Q_{\text{laser}} \quad [17]$$

$$\nabla \cdot \vec{u} = 0 \quad [18]$$

where $\bar{c}_e$, c_1, c_2 are the mixture,[43] metal-phase, and gas-phase specific heat capacities, respectively, J/(kg K); $\bar{k}$ is the mixed thermal conductivity, W/(m K); Q_{laser} is the laser energy density, W/m^3.

If a surface heat source is used, then the extremely high laser energy density can easily cause the calculation to diverge. Thus, a body heat source is required. Considering that the laser action zone was constantly changing during the SLM formation process, we used the following laser energy application: First, the first layer of metal-phase elements directly acting by the laser was obtained based on the distribution of α_1 and the position of the spot center. Second, using the first layer of metal-phase elements as a starting point, the metal-phase elements within a certain distance (which was controlled within 8 μm) were found along the gravity direction. Finally, the laser energy was distributed based on the metal-phase volume fraction of each element, and the sum of the element laser energy percentages in the same horizontal position was guaranteed to be one. The body heat source of the laser energy based on interface tracking was

$$Q_{\text{laser}} = \frac{f_{\Delta z} q_{\text{laser}}}{\Delta z} \quad [19]$$

$$q_{\text{laser}} = \frac{2\eta P_{\text{laser}}}{\pi R^2} \exp\left(-2\frac{(x - x_0 - vt)^2 + (y - y_0)^2}{R^2}\right) \quad [20]$$

where $f_{\Delta z}$ is the percentage of laser energy occupied by the element; Δz is the equivalent length of the element such as the side length of a cube, m; q_{laser} is the surface energy density of the laser that obeys the Gaussian distribution, W/m^2; η is the laser absorption rate; P_{laser} is the laser power, W; R is the spot radius, m; x, y are the horizontal coordinates of the element's center point, m; x_0, y_0 are the horizontal coordinates of the spot's center point, m; v is the scanning speed, m/s. We noted that the molten pool depth was generally about 30 μm, and thus it can be considered that the setting of $f_{\Delta z}$ has a small influence on the molten pool depth.

C. *Calculation Process*

Figure 2 shows the SLM calculation process based on the mesoscopic scale. First, the particle size distribution that satisfied the normal distribution was obtained, and the spreading powder process was calculated using the open-source DEM code Yade. Second, the resulting particle center position and radius data were imported into the 3D geometric modeling software to obtain the CAD model. The mesh model required for the calculation was then obtained by pre-processing (the mesh size was 2.5^3 μm^3), and the molten pool dynamics in the SLM formation process was predicted based on the finite difference method (FDM). Finally, the effects of different process parameters on the SLM single-layer multi-pass process were investigated.

III. RESULTS AND DISCUSSION

According to the above physical modeling and numerical solution process, the corresponding simulation research on the influence of process parameters (line energy density and hatch space) on SLM single-layer multi-pass process was carried out and compared with the experimental results. The computing resource was an Intel Xeon Gold 5120 CPU (32GB RAM, 28 threads), and the time step size was set to 10^{-8} s.

A. *Calculation Parameters*

The material was 316L stainless steel, and its alloy composition (mass percentage) was Fe 65.395, C 0.03, Si 1.0, Mn 2.0, P 0.045, S 0.03, Ni 12.0, Cr 17.0, and Mo 2.5. Table II shows the required physical properties of 316L stainless steel.[42] In addition, the laser spot diameter was 54 μm.

B. *Influence of Line Energy Density on the SLM Formation Process*

To comprehensively consider the influence of laser power and scanning speed on the SLM formation process, the line energy density Q^* was analyzed where $Q^* = P_{\text{laser}}/v$. To facilitate the comparison of the effect of line energy density on the SLM process, the calculation used here was the SLM single-layer single-pass formation process. Figure 3 shows the calculation domain used to analyze the line energy density. The overall size was 1000 μm × 150 μm × 130 μm, where the substrate thickness was 50 μm, and the mesh size was 2.5^3 μm^3. The powder bed distribution in Figure 3 was calculated by Yade wherein the average particle radius was 25 μm, and the half-width of the particle radius (the difference between the average and the maximum or minimum) was 5 μm. The powder bed had a thickness of

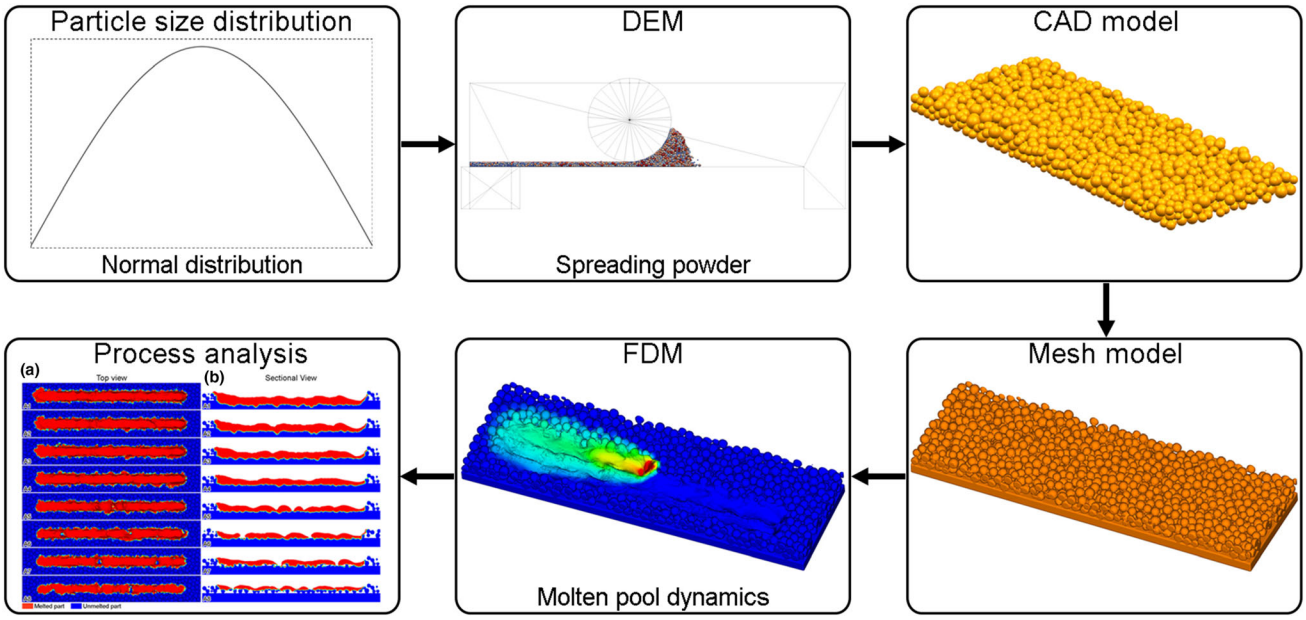

Fig. 2—SLM calculation process based on the mesoscopic scale.

Table II. Physical Properties of 316L Stainless Steel[42]

Parameter	Value	Unit
Density of Solid Metal	7650	kg/m^3
Density of Liquid Metal	6870	kg/m^3
Specific Heat of Solid Metal	596	J/(kg K)
Specific Heat of Liquid Metal	775	J/(kg K)
Thermal Conductivity of Solid Metal	$9.248 + 0.01571T$	W/(m K)
Thermal Conductivity of Liquid Metal	$12.41 + 0.003279T$	W/(m K)
Solidus Temperature	1658	K
Liquidus Temperature	1723	K
Evaporation Temperature	3090	K
Latent Heat of Melting	2.7×10^5	J/kg
Latent Heat of Vaporization	7.45×10^6	J/kg
Viscosity of Liquid Metal	0.00345	Pa s
Surface Tension	1.6	N/m
Temperature Slope of Surface Tension	-8×10^{-4}	N/(m K)
Molecular Mass	9.3×10^{-26}	kg
Ambient Pressure	101,325	Pa
Boltzmann Constant	$1.3806505(24) \times 10^{-23}$	J/K
Emissivity	0.26	
Stefan–Boltzmann Constant	5.67×10^{-8}	$W/(m^2 K^4)$
Laser Absorption Coefficient	0.35	

(In the table, T is the temperature (K)).

50 μm, and the obtained powder bed had a packing density of 58.47 pct. During this calculation, the initial temperature was 300 K, and the laser started moving from the position of the horizontal coordinate (100, 75 μm). It stopped when it reached the defined position (900, 75 μm). The domain was then cooled for 100 μs. In terms of computational efficiency, the average calculation time required for the SLM single-pass example was 8 hour.

Figure 4 shows the simulation results of temperature field and solid fraction distribution at different times when the line energy density was 200 J/m; here, the sectional view is the Y-direction middle section of the calculation domain shown in Figure 3. The side thermal boundary condition was symmetric and had less influence on the temperature field of the molten pool. The metal particles were melted by heat to form a molten pool once the laser began to act on the powder bed; as the laser moved forward, new particles were continuously filled in the front of the molten pool, and the tail of the molten pool gradually cooled down to form a solidified track. A part of the substrate was also melted by heat and solidified. Finally, the laser action area formed a continuous solidified track in the powder bed.

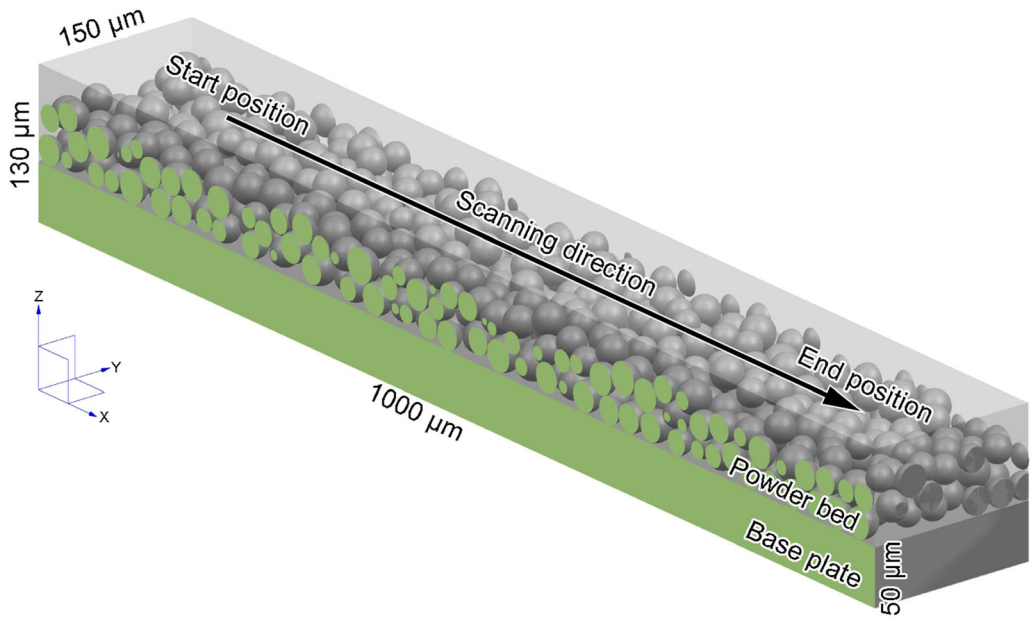

Fig. 3—Computational domain used to analyze line energy density.

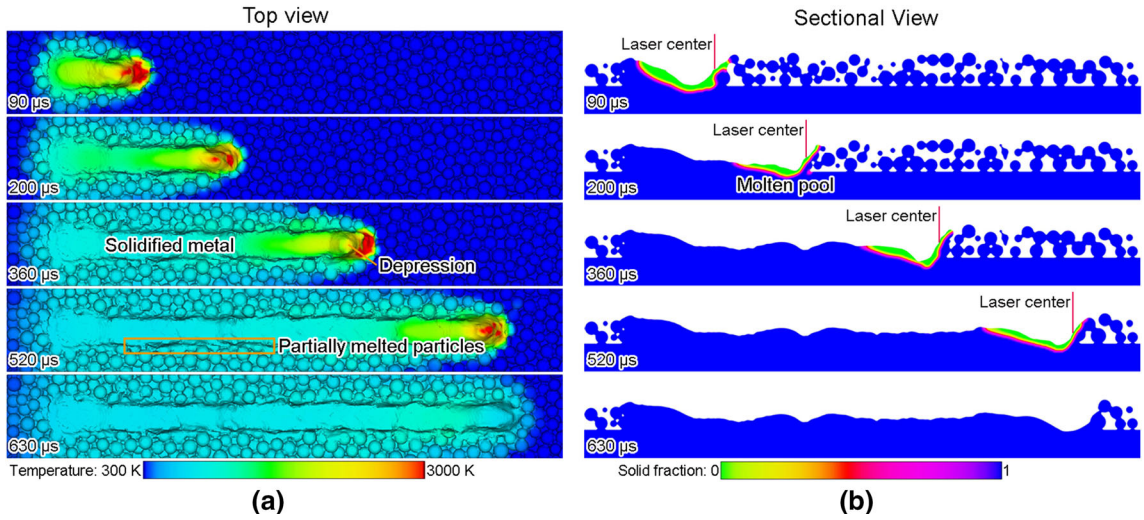

Fig. 4—Simulation results of the temperature field and solid fraction distribution at different times when the line energy density was 200 J/m: (*a*) top view; (*b*) sectional view ($Y = 75$ μm).

We note that there were some partially melted particles on both sides of the solidified track due to the limited area of the laser. Figure 5 shows the local temperature field and velocity field of the mid-section when the line energy density was 200 J/m. The temperature of the molten pool surface at the spot center was the highest since the energy density at the laser spot center was the largest. When the temperature exceeded the metal vaporization temperature, the gasification recoil force was generated in the liquid surface causing a significant downward movement. On the other hand, the Marangoni flow occurred on the liquid surface due to the obvious temperature gradient distribution, i.e., there was flow from the liquid surface region with high temperature to the region with low temperature. Finally, under the combined action of the gasification recoil and Marangoni effect, the molten pool had an obvious concave shape. In addition, significant internal reflow occurred in the back of the molten pool.

To analyze the influence of line energy density on the SLM formation process, the single-pass processes under different line energy densities were calculated. Table 3 shows the calculation schemes for different line energy densities in which the line energy density of the calculation scheme was gradually reduced.

Figure 6 shows the simulation results of the solidified tracks (which were the melted and re-solidified areas) of calculation schemes A1 to A8. Table IV shows the solidified track characteristic data of calculation schemes A1 to A8. The width fluctuation value of

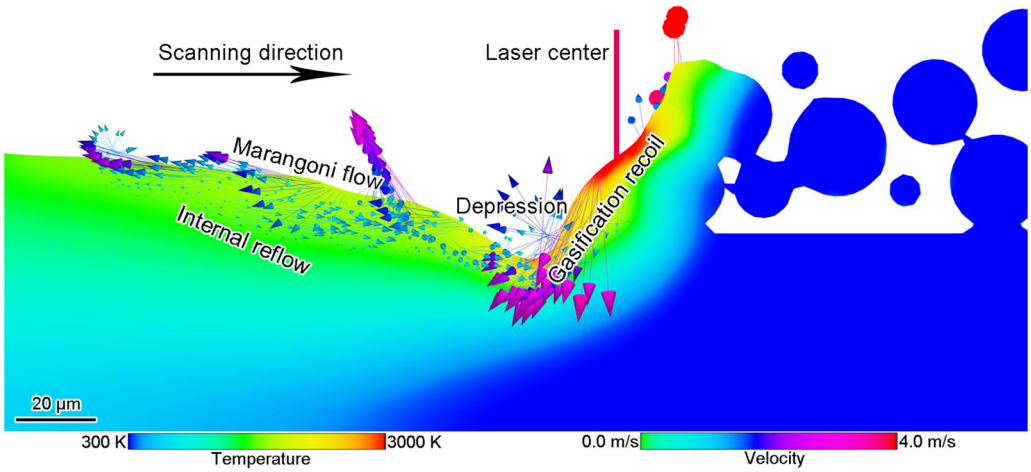

Fig. 5—Local temperature field and velocity field of the mid-section ($Y = 75$ μm) at 50 μs when the line energy density was 200 J/m.

Table III. Calculation Schemes for Analyzing Line Energy Density

Calculation Scheme	Laser Power (W)	Scanning Speed (m/s)	Line Energy Density (J/m)
A1	350	1	350
A2	300	1	300
A3	300	1.5	200
A4	300	2	150
A5	200	1.5	133
A6	200	2	100
A7	200	2.5	80
A8	100	2	50

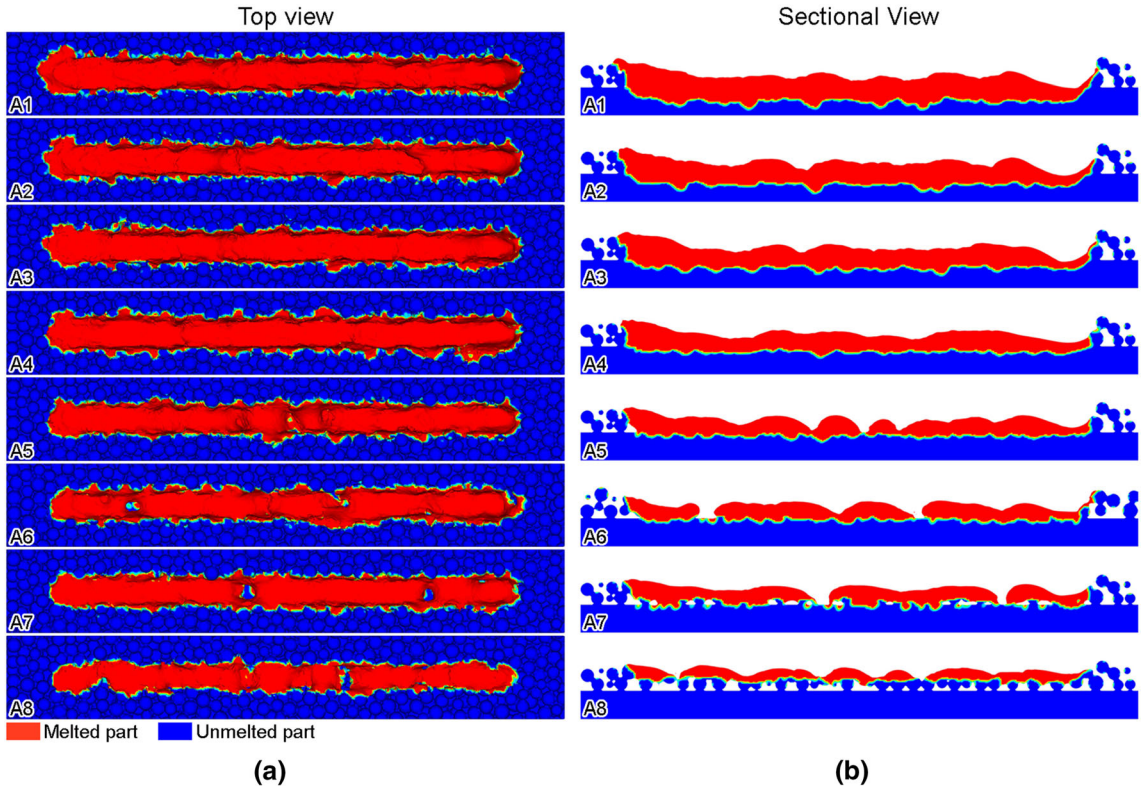

Fig. 6—Simulation results of solidified track morphology of calculation schemes A1 to A8: (*a*) top view; (*b*) sectional view ($Y = 75$ μm).

Table IV. Solidified Track Characteristic Data of Calculation Schemes A1 to A8

Calculation Scheme	Width of Solidified Track (μm)		Upper Surface Coordinate of Solidified Track (μm)		Lower Surface Coordinate of Solidified Track (μm)	
	Average	Fluctuation	Average	Fluctuation	Average	Fluctuation
A1	63.45	8.22	17.99	9.71	− 25.18	10.79
A2	61.90	9.92	22.00	12.00	− 20.40	10.80
A3	63.55	7.89	23.81	8.33	− 15.48	7.54
A4	66.93	11.81	24.59	10.25	− 11.48	8.20
A5	61.02	10.24	20.08	15.75	− 7.87	7.85
A6	discontinuous solidified track					
A7	discontinuous solidified track					
A8	discontinuous solidified track					

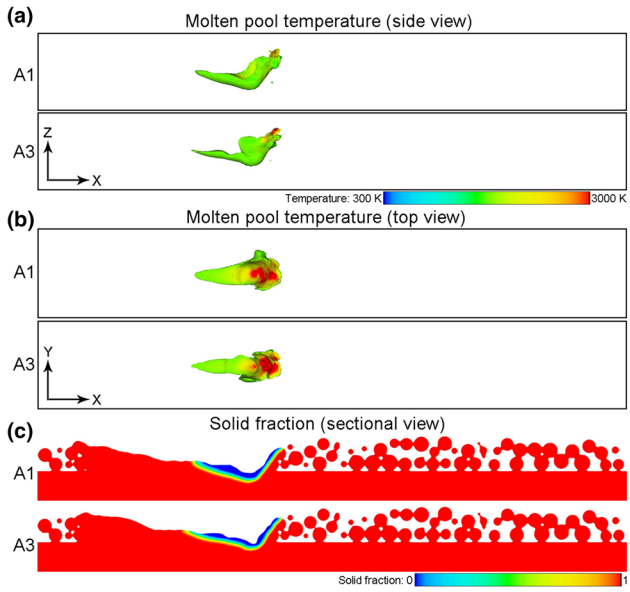

Fig. 7—Simulation results of calculation schemes A1 and A3 when the laser action location was $X = 377.5$ μm: (*a*) the shape of the molten pool (side view); (*b*) the shape of the molten pool (top view); (*c*) the sectional view of the solid fraction ($Y = 75$ μm).

solidified track refers to the variation range of the solidified track boundary in the Y direction. In addition, since the Z-axis coordinate of the substrate upper surface was 0 μm, the upper surface coordinate and the lower surface coordinate of the solidified track represent the contribution of the metal particles and the substrate to the solidified track region, respectively. The comparison results show that the difference in the width of the solidified tracks and its fluctuation at different line energy densities was not significant. The average value of the upper surface coordinate first increased and then decreased as the line energy density increased. The fluctuation value first decreased and then increased indicating that the flatness of the upper surface first became better and then worsened. As the line energy density increased, the average value of the lower surface coordinate gradually increased, and the fluctuation value gradually decreased—these observations suggest that the melted region in the substrate or the former layer was gradually reduced. Table IV does not give solidified track characteristic data of schemes A6 to A8 because the resulting solidified tracks were obviously discontinuous and were not preferable to the actual SLM production; thus, there is no analysis value.

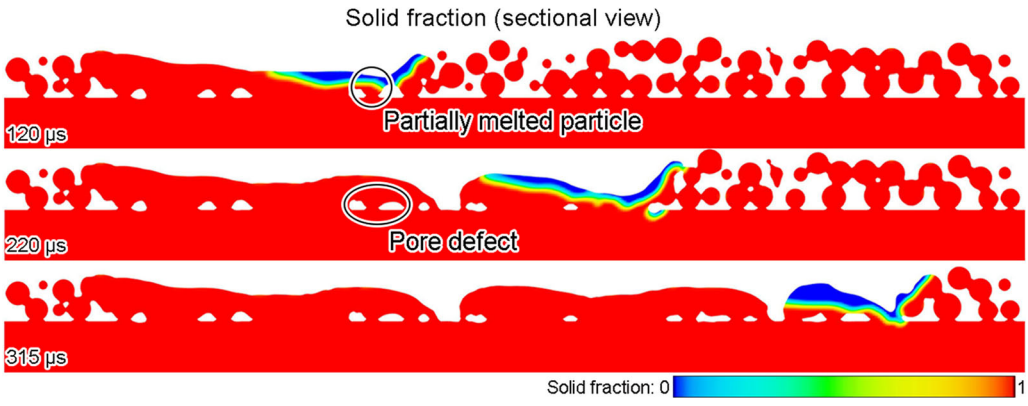

Fig. 8—Sectional view of the solid fraction at different times when the line energy density was 80 J/m ($Y = 75$ μm).

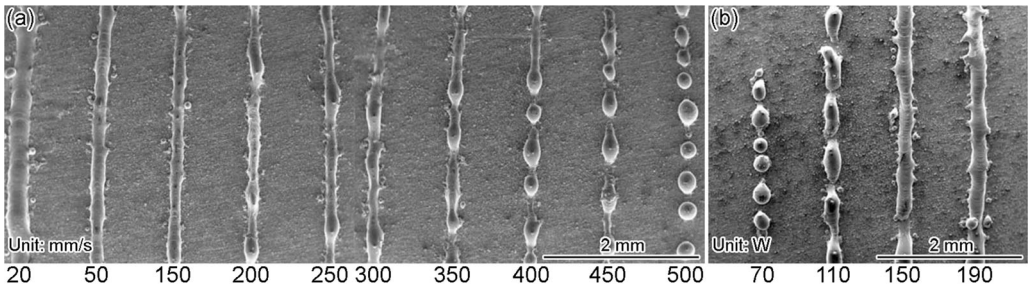

Fig. 9—Experimental results of single-pass SLM tests at different line energy densities, with permission Ref. [48]: (*a*) different scanning speeds; (*b*) different laser powers.

More energy was applied to the powder bed when the line energy density was high, and thus the depth and width of the molten pool were larger (Figure 7). Because the complex flow behavior of the molten pool was affected by the Marangoni effect, gasification recoil, surface tension, and internal reflow, the fluctuation of the molten pool surface was more severe in the case of high line energy density resulting in a less flat solidified track. Concurrently, when the line energy density was high, the substrate or the former layer absorbed more laser energy so that the melted area was larger. We note that when the line energy density is too high, the keyhole phenomenon can cause pore defects; however, the roughness of the solidified track surface at high line energy density was mainly focused here. Thus, the situation of excessive line energy density has not been calculated. Figure 8 shows that the energy applied to the powder bed was low when the line energy density was low—this can lead to partially melted particles in the bottom of the powder bed in the formation zone causing insufficient fusion between the current formation layer and the substrate or the former layer. This in turn led to pore defects. In addition, since the depth and width of the molten pool were small when the line energy density was low, the surface tension had large influence on the molten pool flow. It caused the so-called ball phenomenon leading to a solidified track with an uneven surface or even a discontinuous solidified track. At the same time, the substrate or the former layer absorbed less laser energy when the line energy density was lower. Thus, the melted area was smaller. Figure 9 shows the experimental results of single-pass SLM tests for 316L stainless steel powder at different line energy densities.[48] The experimental results show that the continuous solidified track gradually changed to a discontinuous one as the line energy density decreased. The ball defect eventually occurred, which is consistent with the simulation results.

The characteristic data fluctuation of the ideal SLM solidified track should be as small as possible to obtain a flat formation zone. The lower surface coordinate of the solidified track should be moderate to establish a good connection with the substrate or the former layer. The analysis above shows that an uneven solidified track was obtained when the line energy density was too high or too low. The substrate or the former layer was excessively melted when the line energy density was high. The melted area of the substrate or the former layer was small when the line energy density was low (Figure 10). Therefore, a moderate line energy density should be used to obtain a relatively flat solidified track and establish a good connection with the substrate or the former layer.

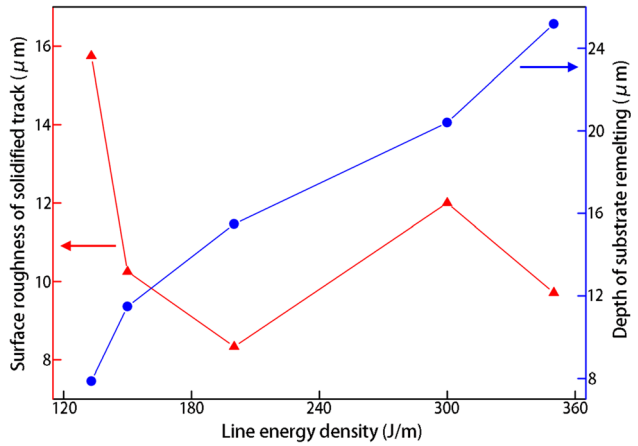

Fig. 10—Surface roughness and depth of substrate re-melting of solidified tracks at different line energy densities.

C. *Influence of Hatch Space on the SLM Formation Process*

To analyze the effect of hatch space on the SLM formation process, the calculation used here was the SLM single-layer multi-pass process. Figure 11 shows the calculation domain used to analyze the hatch space. The overall size was 1000 μm × 400 μm × 110 μm where the substrate thickness was 30 μm, the powder bed thickness was 50 μm, the mesh size was 2.5 μm, and the particle size distribution was consistent with that in Figure 3. During the calculations, the laser was applied in five paths in sequence. During the process of forming each path, the laser moved from the *X*-coordinate 100 μm to *X*-coordinate 900 μm, and the *Y*-coordinate difference of adjacent paths was the hatch space. The laser power and scanning speed were maintained at 240 W and 1.5 m/s. We note that the calculation domain size used herein was limited, and the length of laser single-pass formation in the actual SLM process is often several tens of millimeters. Thus, for the sake of calculation simplicity, the temperature of the calculation domain was set to 300 K when each path was started. In

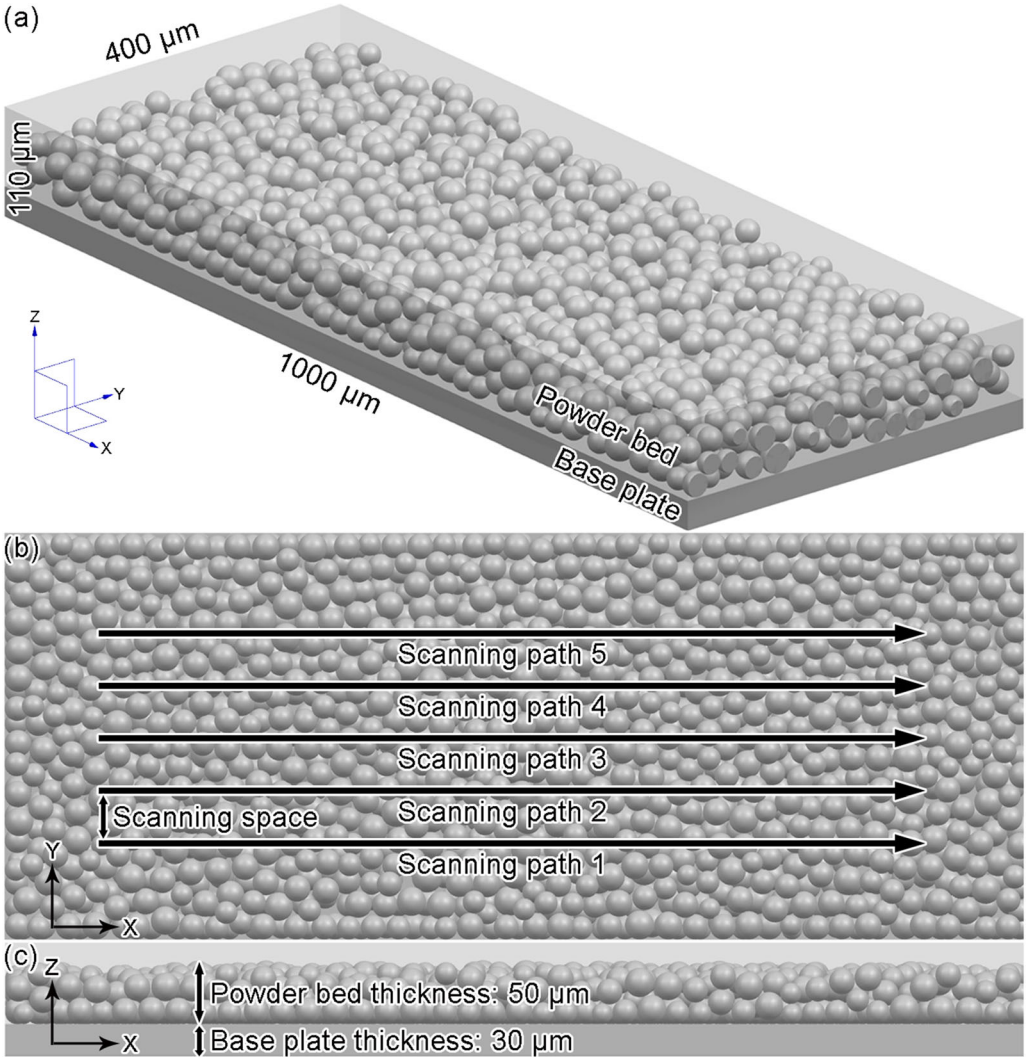

Fig. 11—Computational domain used to analyze hatch space: (*a*) three-dimensional view; (*b*) top view; (*c*) side view.

terms of computational efficiency, the average calculation time required for the SLM single-layer multi-pass example was 70 hour.

Figure 12 shows the temperature field and solid fraction distribution of the formation zone at different times when the hatch space was 45 μm. The calculation results show that the metal particles were melted by the laser irradiation to form a molten pool. As the laser spot moved continuously, the molten pool also moved under the combined effects of laser energy absorption, internal heat convection, heat radiation, and heat transfer with the solid-phase region. The temperature of the laser-applied area was significantly higher than that of the untreated area, and the shape of the molten pool was raindrop-shaped. In addition, the comparison found that the surface morphology of the solidified track and the molten pool shape at different times were different because the particle distribution in different regions of the powder bed was difficult to maintain. This lack of control affected the local molten pool evolution behavior. Figure 13 shows the shapes of the solidified track on different *Y*-direction sections (mid-sections in each solidified track) at a hatch space of 45 μm. The shapes of the respective solidified tracks were different because the particle distributions on the respective paths differed from each other. However, the average values of the upper and lower surface coordinates of the solidified tracks were substantially the same, and each solidified track established a good connection with the substrate or the former layer.

Figure 14 shows the shapes of the solidified track obtained by forming each path at the hatch space of 45 μm. The results show that the width of the solidified track obtained from the second to fifth paths was significantly larger than the width obtained from the first path (Figure 15). This is because the areas where the laser did not act in the first path were all deposited particles, and there were voids between the particles. This in turn formed a thermal resistance to hinder the heat transfer; however, the molten pool was always overheated, and thus when forming the subsequent paths, one side of the laser action area was the continuous solid metal with better thermal conductivity than the deposited particles. The adjacent solidified

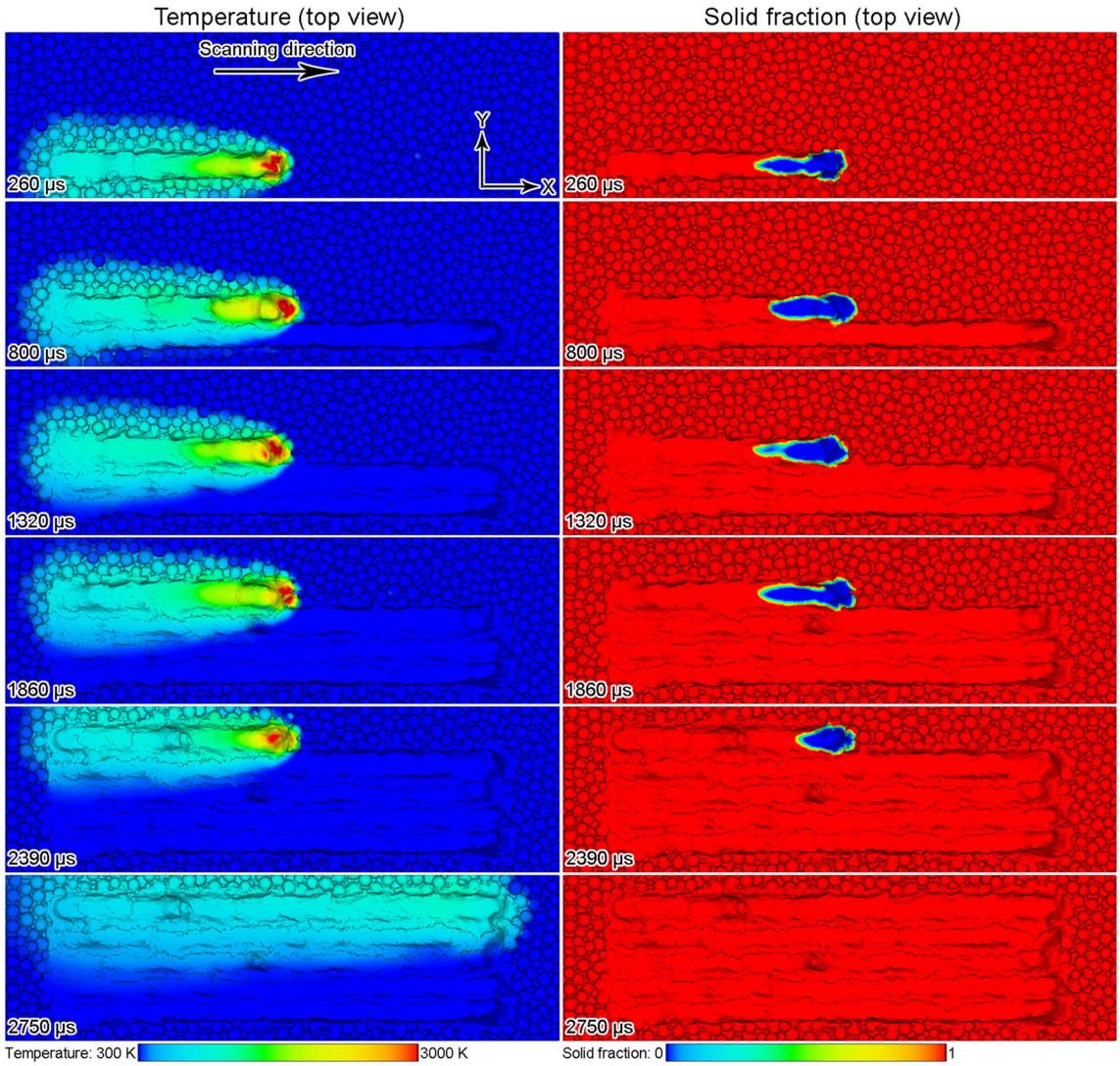

Fig. 12—Temperature field and solid fraction distribution at different times when the hatch space was 45 μm (top view).

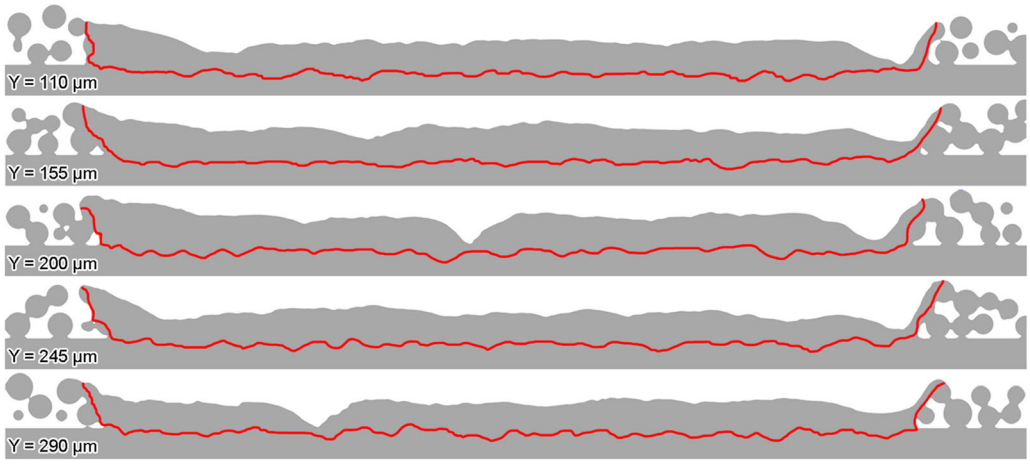

Fig. 13—Shapes of the solidified track on different *Y*-direction sections at the hatch space of 45 μm (red curves represent the boundary of the solidified track) (Color figure online).

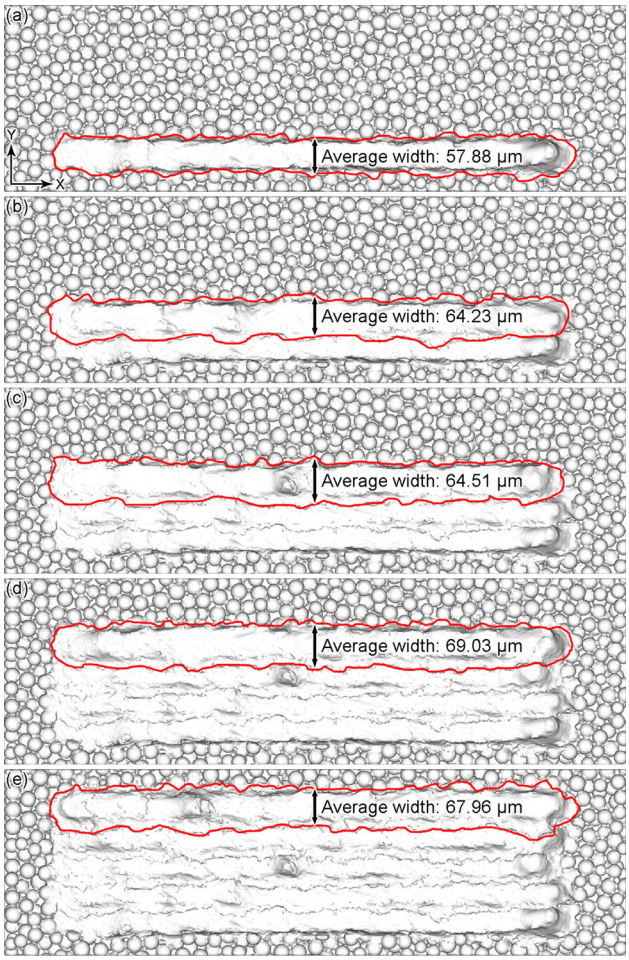

Fig. 14—Shapes of the solidified track obtained by forming each path at the hatch space of 45 μm (top view, red curves represent the boundary of the solidified track): (*a*) first path; (b) second path; (*c*) third path; (*d*) fourth path; (*e*) fifth path (Color figure online).

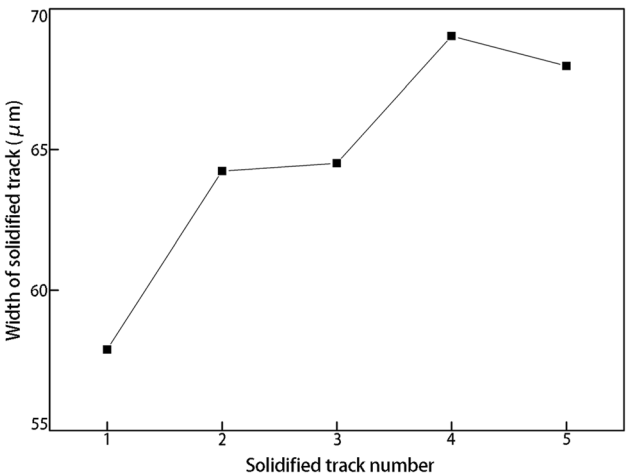

Fig. 15—Width of each solidified track.

track then partially re-melted, which made the current solidified track width larger. Figure 16 shows a collection of the boundaries of each solidified track in Figure 14, wherein the curves with different colors represent different solidified track boundaries. Figure 16 shows that there were significant overlaps between adjacent solidified tracks, which means that partial melting of the adjacent melt channel occurred when a certain solidified track was formed. This plays a key role in establishing good connections between adjacent solidified tracks.

To analyze the influence of hatch space on the SLM formation process, the single-layer multi-pass processes under different hatch spaces were calculated here. Table V shows the calculation schemes at different hatch spaces in which the hatch space was gradually reduced.

Figure 17 shows the boundaries of the solidified tracks at different hatch spaces. It is obvious from the comparison results that the overlapping area between adjacent solidified tracks was limited or even not overlapping at all when the hatch space was large (hatch space of 65 μm, Table VI). As the hatch space gradually reduced, the overlapping area between adjacent solidified tracks was gradually increased (the overlap widths were 10.42, 21.76, and 34.75 μm when the hatch spaces were 55, 45, and 35 μm, respectively, Table VI). The average width of the overlap area reached 34.75 μm when the hatch space was 35 μm. This exceeded the laser spot radius (27 μm) meaning that the first path and third path, second path and fourth path, and third path and fifth path overlapped. Since excessive overlap of adjacent solidified tracks implies a decrease in production efficiency, appropriate overlap of adjacent solidified tracks should occur during the ideal SLM multi-pass process to strike a balance between production efficiency and a good connection between the solidified tracks.

Figure 18 shows the three-dimensional shapes of the formation zone at different hatch spaces. The calculation results here were raised regions between adjacent solidified tracks. The size of the raised regions was large when the hatch space was large. Figure 19 shows cross-sectional views of the formation zone at different hatch spaces, and the data in the raised regions of Table VI indicate that when the hatch space were 35 and 45 μm, the height and width of the raised regions between the solidified tracks were significantly smaller. Here, the generation of the raised region was caused by Marangoni flow on the liquid surface of the molten pool so that the liquid in the central portion was dispersed to the periphery, and the solidified track morphology with a high edge was formed during the solidification process. The height and width of the raised region between the solidified tracks were significantly larger when the hatch space was 55 and 65 μm. At this time, the generation of the raised region was mainly due to the limited overlapping area between adjacent solidified tracks so that the particles between the solidified tracks were not sufficiently melted, thereby forming a large raised region. Figure 20 shows the experimental results of multi-pass SLM tests for 316L stainless steel powder at different hatch spaces.[48] The results show that when the hatch space was small, adjacent solidified tracks formed a dense metallurgical bond. When the hatch space was

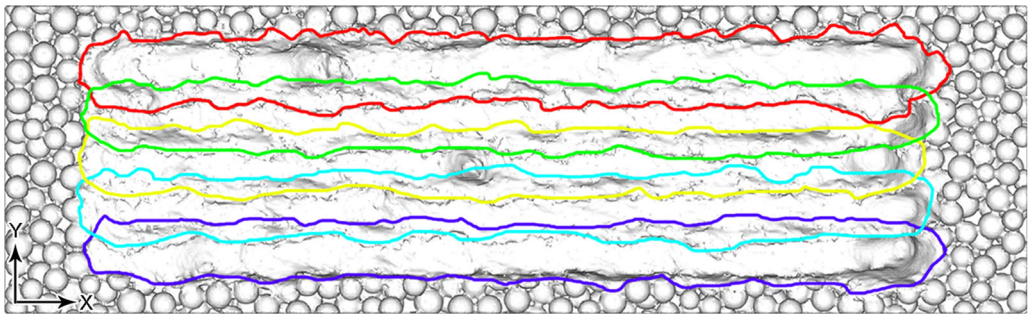

Fig. 16—Collection of the boundaries of each solidified track at the hatch space of 45 μm (curves with different colors represent different solidified track boundaries).

Table V. Calculation Scheme for Analyzing the Hatch Space

Calculation Scheme	Hatch Space (μm)
B1	65
B2	55
B3	45
B4	35

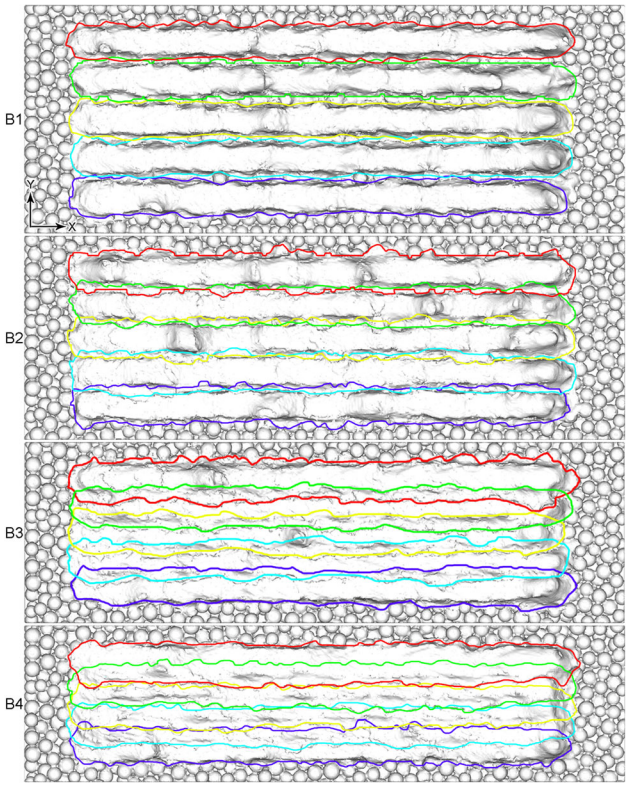

Fig. 17—Boundaries of the solidified tracks at different hatch spaces (curves with different colors represent different solidified track boundaries).

large, regular gaps appeared between adjacent solidified tracks because some of the metal particles between adjacent solidified tracks were not subjected to laser action. Thus, they were removed during the cleaning process after formation was complete. This led to a gap. It is difficult to consider the cleaning of the formation zone by the numerical calculation, and thus the solidified track morphology obtained by simulation was different from the experimental results. Nevertheless, the conclusions were consistent. In the ideal SLM multi-pass process, the surface of the formation zone should be as flat as possible to facilitate laying powder of the next formation layer and to obtain a good surface topography. Based on the above analysis, from the viewpoint of controlling hatch space, it should satisfy three conditions: establishing the good connection of adjacent solidified tracks, obtaining the relatively flat formation surface, and high production efficiency in the actual SLM production.

IV. CONCLUSIONS

(1) The random particle distribution of the powder bed was obtained *via* the open-source DEM code Yade wherein the particle size distribution satisfied a normal distribution.
(2) The prediction model of the molten pool dynamic behavior during the SLM process was established based on the "metal-gas" two-phase flow model. The conservation equation considered the thermal factors such as Marangoni effect, the porosity in the mushy zone, and the gasification phenomenon. The laser energy was applied by the body heat source model, which tracked the metal-phase surface directly affected by the laser in real time. The energy applied to the metal-phase elements within a certain thickness.
(3) From the viewpoint of controlling line energy density for 316L stainless steel, 200 J/m should be used to obtain a relatively flat solidified track and establish a good connection with the substrate or the former layer.
(4) From the viewpoint of controlling hatch space for 316L stainless steel, 45 μm should be used to satisfy three conditions: establishing the good connection of adjacent solidified tracks, obtaining a relatively flat formation surface, and high production efficiency.

Table VI. Characteristic Data of the Formation Zones at Different Hatch Spaces

Hatch Space (μm)	Overlap Width Between Adjacent Solidified Tracks (μm)	Height of the Raised Region Between the Solidified Tracks (μm)	Width of the Raised Region Between the Solidified Tracks (μm)
65	not overlapping	27.88	33.91
55	10.42	17.44	33.54
45	21.76	5.84	23.94
35	34.75	4.31	17.46

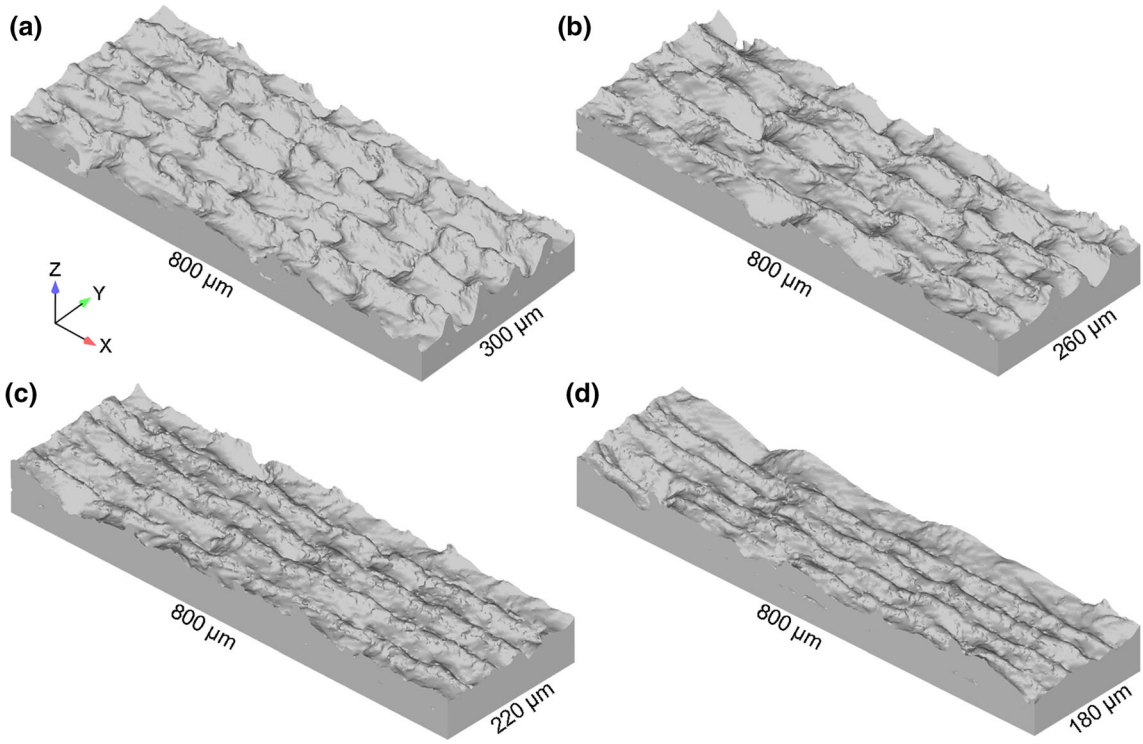

Fig. 18—Three-dimensional shapes of the formation zone at different hatch spaces: (*a*) B1; (*b*) B2; (*c*) B3; (d) B4.

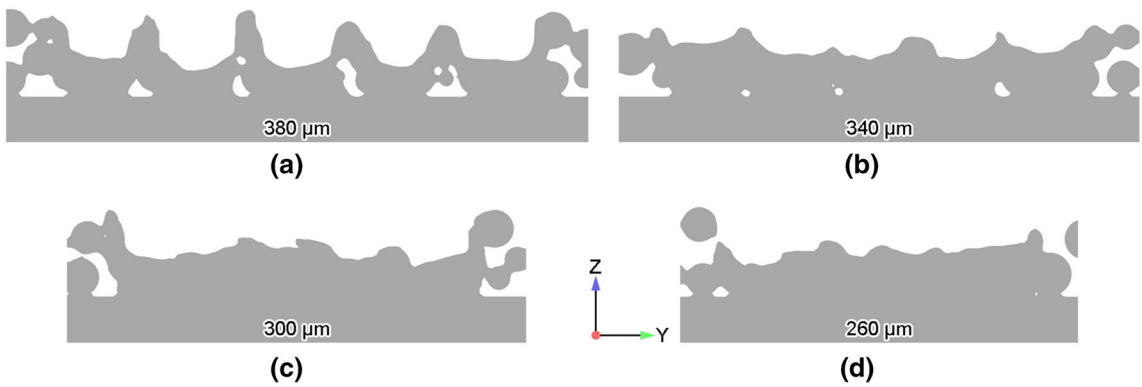

Fig. 19—Cross-sectional views of the formation zone at different hatch spaces: (*a*) B1; (*b*) B2; (*c*) B3; (*d*) B4.

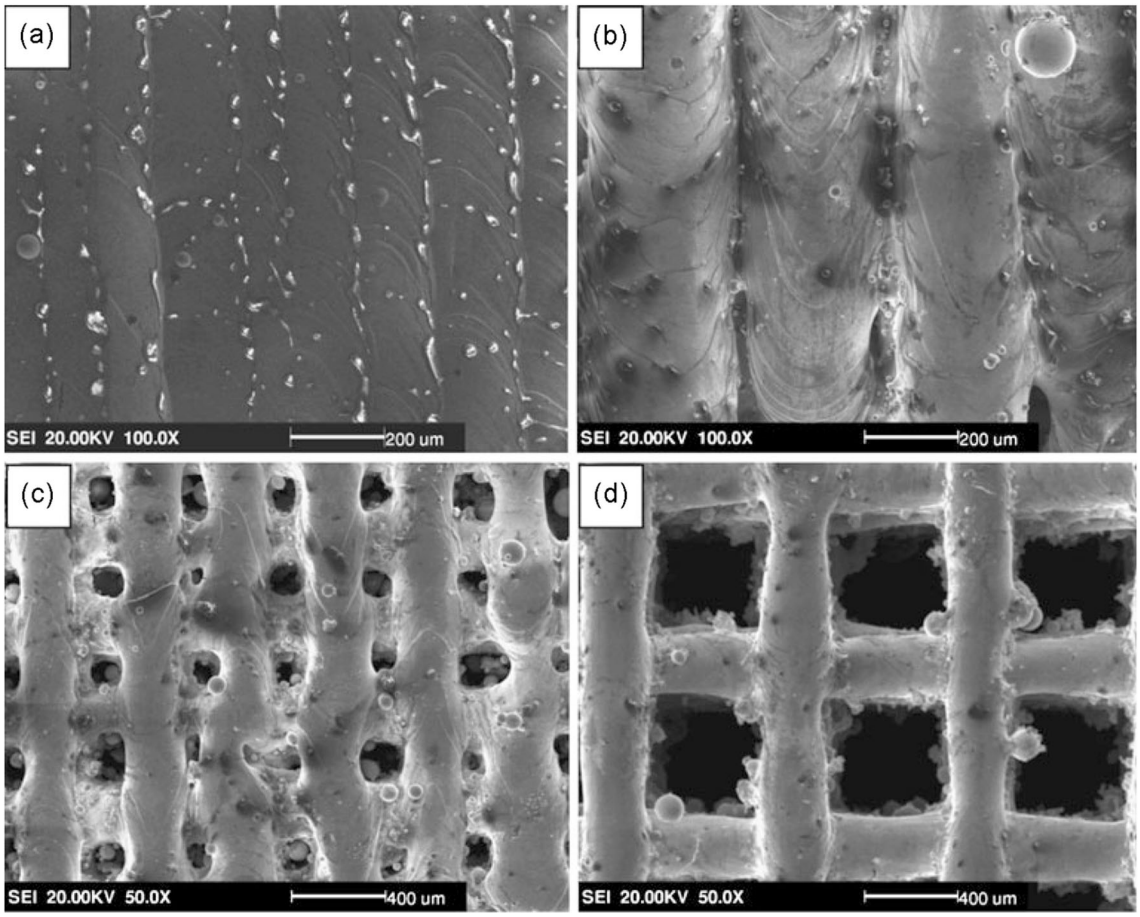

Fig. 20—Experimental results of multi-pass SLM tests at different hatch spaces, with permission Ref. [48]: (*a*) 0.15 mm; (*b*) 0.3 mm; (*c*) 0.4 mm; (*d*) 0.8 mm.

ACKNOWLEDGMENTS

This work was supported by the Natural Science Foundation of Guangdong Province (No. 2019A1515012040) and the Research Platform Construction Funding of Advanced Institute of Engineering Science for Intelligent Manufacturing, Guangzhou University.

REFERENCES

1. C. Zitelli, P. Folgarait, and A.D. Schino: *Metals*, 2019, vol. 9 (7), art. no. 731.
2. J.L. Zhang, B. Song, Q.S. Wei, D. Bourell, and Y.S. Shi: *J. Mater. Sci. Technol.*, 2019, vol. 35 (2), pp. 270–84.
3. H. Shipley, D. McDonnell, M. Culleton, R. Coull, R. Lupoi, G. O'Donnell, and D. Trimble: *Int. J. Mach. Tool. Manuf.*, 2018, vol. 128, pp. 1–20.
4. S. Shrestha, T. Starr, and K. Chou: *J. Manuf. Sci. E.*, 2018, vol. 141 (7), art. no. 071004.
5. M. Grasso, A.G. Demir, B. Previtali, and B.M. Colosimo: *Robot. Com.-Int. Manuf.*, 2018, vol. 49, pp. 229–39.
6. C.L.A. Leung, S. Marussi, R.C. Atwood, M. Towrie, P.J. Withers, and P.D. Lee: *Nat. Commun.*, 2018, vol. 9 (1), art. no. 1355.
7. R. Laquai, B.R. Müller, G. Kasperovich, J. Haubrich, G. Requena, and G. Bruno: *Mater. Res. Lett.*, 2018, vol. 6 (2), pp. 130–35.
8. B. AlMangour, D. Grzesiak, T. Borkar, and J.M. Yang: *Mater. Des.*, 2018, vol. 138, pp. 119–28.
9. D.H. Dai, D.D. Gu, H. Zhang, J.P. Xiong, C.L. Ma, C. Hong, and R. Poprawe: *Opt. Laser Technol.*, 2018, vol. 99, pp. 91–100.
10. W.T. Shi, P. Wang, Y.D. Liu, Y.J. Hou, and G.L. Han: *Powder Technol.*, 2020, vol. 360, pp. 151–64.
11. J.W. Liu, Y.N. Song, C.Y. Chen, X.B. Wang, H. Li, C.A. Zhou, J. Wang, K. Guo, and J. Sun: *Mater. Des.*, 2020, vol. 186, art. no. 108355.
12. O.O. Salman, F. Brenne, T. Niendorf, J. Eckert, K.G. Prashanth, T. He, and S. Scudino: *J. Manuf. Process.*, 2019, vol. 45, pp. 255–61.
13. Z.Y. Zhang, B.B. Chu, L. Wang, and Z.H. Lu: *J. Alloy. Compd.*, 2019, vol. 791, pp. 166–75.
14. M. Laleh, A.E. Hughes, W. Xu, I. Gibson, and M.Y. Tan: *Corros. Sci.*, 2019, vol. 155, pp. 67–74.
15. T. Larimian, M. Kannan, D. Grzesiak, B. AlMangour, and T. Borkar: *Mater Sci. Eng. A*, 2020, vol. 770, art. no. 138455.
16. Y. Yang, Y. Zhu, M.M. Khonsari, and H. Yang: *Wear*, 2019, vol. 428, pp. 376–86.
17. S.L. Sing, F.E. Wiria, and W.Y. Yeong: *Robot. Com.-Int. Manuf.*, 2018, vol. 49, pp. 170–80.
18. Z.F. Xiao, Y.Q. Yang, R. Xiao, Y.C. Bai, C.H. Song, and D. Wang: *Mater. Des.*, 2018, vol. 143, pp. 27–37.
19. O.O. Salman, C. Gammer, J. Eckert, M.Z. Salih, E.H. Abdulsalam, K.G. Prashanth, and S. Scudino: *Mater. Today Commun.*, 2019, vol. 21, art. no. 100615.
20. Z.Y. Zhao, J. Li, P.K. Bai, H.Q. Qu, M.J. Liang, H.H. Liao, L.Y. Wu, .PC. Huo, H. Liu, and J.X. Zhang: *Metals*, 2019, vol. 9 (2), art. no. 267.
21. T.L. Zhong, K.T. He, H.X. Li, and L.C. Yang: *Mater. Des.*, 2019, vol. 181, art. no. 108076.
22. C. Wei, Z. Sun, Q. Chen, Z. Liu, and L. Li: *J. Manuf. Sci. E.*, 2019, vol. 141 (8), art. no. 081014.

23. A.A. Martin, N.P. Calta, S.A. Khairallah, J. Wang, P.J. Depond, A.Y. Fong, V. Thampy, G.M. Guss, A.M. Kiss, and K.H. Stone: *Nat. Commun.*, 2019, vol. 10 (1), art. no. 1987.
24. S.L. Sing, F.E. Wiria, and W.Y. Yeong: *Int. J. Refract. Met. Hard Mater.*, 2018, vol. 77, pp. 120–27.
25. O. Andreau, I. Koutiri, P. Peyre, J. Penot, N. Saintier, E. Pessard, T.D. Terris, C. Dupuy, and T. Baudin: *J. Mater. Process. Tech.*, 2019, vol. 264, pp. 21–31.
26. M.M. Francois, A. Sun, W.E. King, N.J. Henson, D. Tourret, C.A. Bronkhorst, N.N. Carlson, C.K. Newman, T. Haut, and J. Bakosi: *Curr. Opin. Solid St. M.*, 2017, vol. 21, pp. 198–206.
27. Y.L. Li, K. Zhou, P.F. Tan, S.B. Tor, C.K. Chua, and K.F. Leong: *Int. J. Mech. Sci.*, 2018, vol. 136, pp. 24–35.
28. S. Roy, M. Juha, M.S. Shephard, and A.M. Maniatty: *Comput. Mech.*, 2018, vol. 62 (3), pp. 273–84.
29. B. Ahmad, S.O.V.D. Veen, M.E. Fitzpatrick, and H. Guo: *Addit. Manuf.*, 2018, vol. 22, pp. 571–82.
30. Y.C. Wu, C.H. San, C.H. Chang, H.J. Lin, R. Marwan, S. Baba, and W.S. Hwang: *J. Mater. Process. Tech.*, 2018, vol. 254, pp. 72–78.
31. S.W. Liu, .HH. Zhu, G.Y. Peng, J. Xin, and X.Y. Zeng: *Mater. Des.*, 2018, vol. 142, pp. 319–28.
32. H.C. Tran and Y.L. Lo: *J. Mater. Process. Tech.*, 2018, vol. 255, pp. 411–25.
33. L. Cao and X.F. Yuan: *Materials*, 2019, vol. 12 (14), art. no. 2272.
34. T. Bartel, I. Guschke, and A. Menzel: *Comput. Math. Appl.*, 2019, vol. 78 (7), pp. 2267–81.
35. Z.K. Wang, W.T. Yan, W.K. Liu, and M.B. Liu: *Comput. Mech.*, 2019, vol. 63 (4), pp. 649–61.
36. C. Panwisawas, C.L. Qiu, M.J. Anderson, Y. Sovani, R.P. Turner, M.M. Attallah, J.W. Brooks, and H.C. Basoalto: *Comp. Mater. Sci.*, 2017, vol. 126, pp. 479–90.
37. Q.Q. Han, H. Gu, and R. Setchi: *Powder Technol.*, 2019, vol. 352, pp. 91–102.
38. E.J.R. Parteli and T. Pöschel: *Powder Technol.*, 2016, vol. 288, pp. 96–102.
39. S.A. Khairallah, A.T. Anderson, A. Rubenchik, and W.E. King: *Acta Mater.*, 2016, vol. 108, pp. 36–45.
40. M.J. Xia, D.D. Gu, G.Q. Yun, D.H. Dai, H.Y. Chen, and Q.M. Shi: *Int. J. Mach. Tool. Manuf.*, 2017, vol. 116, pp. 96–106.
41. W. Nan and M. Ghadiri: *Powder Technol.*, 2019, vol. 342, pp. 801–07.
42. C. Tang, J.L. Tan, and C.H. Wong: *Int. J. Heat Mass Transf.*, 2018, vol. 126, pp. 957–68.
43. L. Cao: *Int. J. Heat Mass Transf.*, 2019, vol. 141, pp. 1036–48.
44. A. Albaba, S. Lambert, F. Nicot, and B. Chareyre: *Granul. Matter*, 2015, vol. 17 (5), pp. 603–16.
45. L. Cao: *Int. J. Adv. Manuf. Tech.*, 2019, vol. 105, pp. 2253–69.
46. L. Cao, D.M. Liao, F. Sun, T. Chen, Z.H. Teng, and Y.L. Tang: *Int. J. Adv. Manuf. Tech.*, 2017, vol. 94, pp. 807–15.
47. L. Cao, F. Sun, T. Chen, Z.H. Teng, Y.L. Tang, and D.M. Liao: *Acta Metall. Sin.*, 2017, vol. 53 (11), pp. 1521–11.
48. R.D. Li, J.H. Liu, Y.S. Shi, L. Wang, and W. Jiang: *Int. J. Adv. Manuf. Tech.*, 2012, vol. 59 (9–12), pp. 1025–35.